

Contents

1	1 Charge monitoring	
2	<i>The ATLAS Diamond Beam Monitor</i>	2
3	1.1 Introduction	2
4	1.2 Luminosity measurements	3
5	1.3 Diamond pixel module	4
6	1.3.1 Sensors	4
7	1.3.2 Front-end electronics	4
8	1.4 Module assembly	7
9	1.5 Performance results	7
10	1.5.1 Source test results	7
11	1.5.2 Erratic current	11
12	1.5.3 Test beam results	11
13	1.5.4 Summary of the QC	12
14	1.6 Installation and commissioning	13
15	1.6.1 Positioning in ATLAS	14
16	1.7 First data taking during collisions	15
17	1.7.1 LHC beam bunch structure	15
18	1.7.2 Collision point reference system	15
19	1.7.3 Discussion	16
20	1.8 Conclusion	17

²² **Chapter 1**

²³ **Charge monitoring**

²⁴ ***The ATLAS Diamond Beam Monitor***

²⁵ **1.1 Introduction**

²⁶ Particle detectors in high energy physics experiments need to meet very stringent specifications,
²⁷ depending on the functionality and their position in the experiment. In particular, the detectors
²⁸ in the core of the experiment close to the collision point are subject to high levels of radiation. In
²⁹ addition, they need to operate with a high spatial and temporal segmentation to be able to precisely
³⁰ measure trajectories of hundreds of particles within nanoseconds. In addition, they need to be highly
³¹ efficient. In terms of the structure, their active sensing material has to be thin so as not to cause
³² the particles to scatter or get stopped, which would worsen the measurements. This also means
³³ that they have to have a low heat dissipation so that the cooling system can be minimised or even
³⁴ avoided. Finally, they need to be able to have a stable operation for several years without a required
³⁵ intervention, because they are buried deep under tonnes of material and electronics.

³⁶ The material of choice for the inner detector layers in the HEP experiments is silicon. It can
³⁷ withstand high doses of radiation, it is highly efficient (of the order of $\sim 99.9\%$) and relatively low
³⁸ cost due to using existing industrial processes for its production. Its downside is that, with increasing
³⁹ irradiation levels, it needs to be cooled to increasingly low temperatures to ensure a stable operation.
⁴⁰ This is not the case with diamond. In addition, diamond has a lower radiation damage factor, which
⁴¹ means it can operate in a radiation-heavy environment for a longer period.

⁴² The ATLAS Diamond Beam Monitor (the DBM) [13] is a novel high energy charged particle
⁴³ detector. Its function is to measure luminosity (described in section 1.2) and beam background
⁴⁴ (particles not originating in the collision point) in the ATLAS experiment. Given its position in
⁴⁵ a region with a high radiation dose, diamond was chosen as the sensing material. The monitor's
⁴⁶ pCVD diamond sensors are instrumented with pixellated FE-I4 front-end chips. The pCVD diamond
⁴⁷ sensor material was chosen to ensure the durability of the sensors in a radiation-hard environment
⁴⁸ and the size of its active area. The DBM is not the first diamond detector used in HEP, but it is the
⁴⁹ largest pixellated detector installed thus far, as shown in figure 1.1. It was designed as an upgrade to
⁵⁰ the existing luminosity monitor called the Beam Conditions Monitor (BCM) [9] consisting of eight
⁵¹ diamond pad detectors. The BCM is able to perform precise time-of-flight (ToF) measurements.
⁵² The DBM complements the BCM's features by implementing tracking capability. Its pixelated front-
⁵³ end electronics significantly increase the spatial resolution of the system. Furthermore, the DBM is
⁵⁴ able to distinguish particle tracks originating in the collision region from the background hits. This

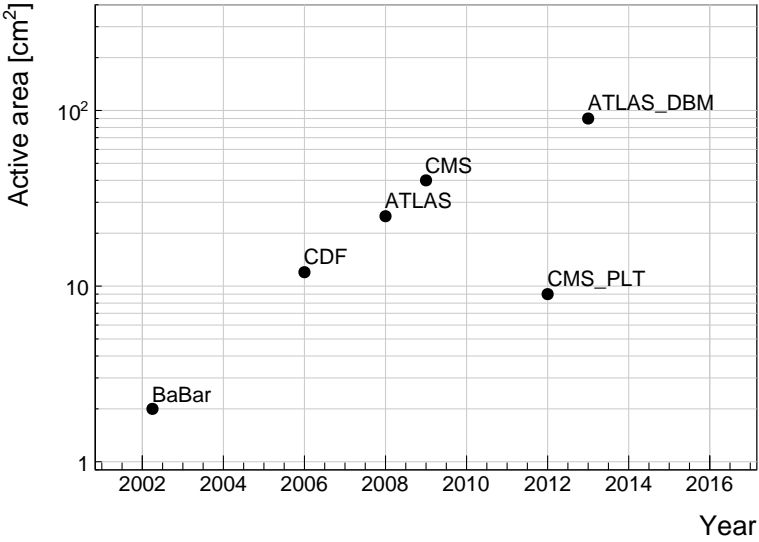


Figure 1.1: Diamond detectors installed in high-energy physics experiments in the last decade, sorted by the active sensor area. The first four detectors from the left are radiation monitors whereas the right two are pixel trackers.

55 capability is a result of its projective geometry pointing towards the interaction region. This chapter
56 first describes the principles of luminosity measurements. It then explains how the DBM carries out
57 this task. Finally, some results from the commissioning and from the real collisions are presented.

58 When a particle traverses a sensor plane, a hit is recorded in the corresponding pixel. Thus, a
59 precise spatial and timing information of the hit is extracted. With three or more sensors stacked
60 behind each other, it is also possible to define the particle's trajectory. This is the case with the
61 DBM. Its projective geometry allows the particles to be tracked if they traverse the sensor planes.
62 The DBM relates the luminosity to the number of particle tracks that originate from the collision
63 region of the ATLAS experiment. Particles that hit the DBM from other directions are rejected as
64 background radiation.

65 1.2 Luminosity measurements

66 Luminosity is one of the most important parameters of a particle collider. It is a measurement of the
67 rate of particle collisions that are produced by two particle beams. It can be described as a function
68 of the beam parameters, such as: the number of colliding bunch pairs, the revolution frequency, the
69 number of particles in each bunch and the transverse bunch dimensions. The first four parameters
70 are well defined. However, the transverse bunch dimensions have to be determined experimentally
71 during calibration measurements. The ATLAS experiment uses the *van der Meer scan* [3] during
72 low-luminosity runs to calibrate the luminosity detectors. This scan is performed by displacing one
73 beam in a given direction and measuring the rate of interactions as a function of the displacement.
74 The transverse charge density of the bunches can be estimated on the basis of the interaction rate.
75 The calibrated luminosity detectors can then operate during high-luminosity runs.

76 One approach to luminosity monitoring is to count the number of particles produced by the
77 collisions. The luminosity is then proportional to the number of detected particles. A detector has
78 to be capable of distinguishing individual particles that fly from the interaction point through the

1.3. DIAMOND PIXEL MODULE

79 active sensor area. If the detector has at least three layers, it can reconstruct the particles' tracks,
80 which in turn yields more information on the their trajectory. This is one reason why detectors
81 with a high timing- and spatial segmentation are more suitable for these applications. The second
82 reason is that, with a high spatial segmentation, the detector does not saturate even at high particle
83 fluencies.

84 1.3 Diamond pixel module

85 The two most important parts of the diamond pixel module are the sensor, which translates the
86 incident ionising radiation into charge carriers as explained in chapter ??, and the pixellated front-
87 end chip, which collects the ionised charge with a high spatial segmentation, processes the recorded
88 data and sends them to the readout system. This section describes these two parts of the module
89 and their interconnection.

90 1.3.1 Sensors

91 The DBM modules are instrumented with two types of sensors – pCVD diamond and silicon. The
92 silicon sensors are used as a fallback solution because there were not enough high-quality diamond
93 sensors available during the construction phase. In addition, a comparative study of irradiation
94 damage between silicon and diamond can be made with such a hybrid system.

95 **Diamond sensors** The target material for this application is pCVD diamond. The reason for this
96 is that the active area of an individual sensor must be approximately $2\text{ cm} \times 2\text{ cm}$, which is too
97 large for the sCVD diamond (maximum sizes available are $10\text{ mm} \times 10\text{ mm}$). pCVD material is also
98 a bit cheaper, which makes a detector with a large active area more feasible to build. The material
99 is provided by three companies: DDL, E6 and II-IV and it is grown in 15 cm wafers, as seen in
100 figure 1.2. The target thickness of the wafers is $500\text{ }\mu\text{m}$. The minimum required charge collection
101 efficiency is 40 % ($\text{CCD} \geq 200\text{ }\mu\text{m}$) to ensure that the MPV of the collected charge for MIPs is still
102 well above the noise of the electronics even after heavy irradiation. They need to be operated at
103 bias voltages between $600\text{ V} - 1'000\text{ V}$. On one side there is a single gold electrode applied across
104 the entire surface. On the other side a pixellated metallisation is added.

105 **Silicon sensors** are standard $n^+ - in - n$ planar sensors with a $200\text{ }\mu\text{m}$ thickness and were fabricated
106 at CiS [1], a company from Erfurt, Germany. They are designed to have nearly a 100 % efficiency
107 when not irradiated. One side is segmented into pixels. Guard rings at the edges of the sensor
108 provide a controlled drop in potential, reducing the possibility of shorts at maximum design bias
109 voltages of the order of $1'000\text{ V}$.

110 1.3.2 Front-end electronics

111 The FE-I4 (front-end version four) [4] is an ASIC pixel chip designed specifically for the ATLAS
112 pixel detector upgrade. It is built as a successor to the current pixel chip FE-I3, surpassing it in size
113 of the active area ($6\times$ larger) as well as the number of channels/pixels ($10\times$ more). 336 such FE-I4
114 modules are used in the newly installed pixel layer called the Insertable B-Layer (IBL) [10]. The
115 DBM is also instrumented with these chips. The FE-I4's integrated circuit contains readout circuitry
116 for $26'880$ pixels arranged in 80 columns on a $250\text{ }\mu\text{m}$ pitch and 336 rows on a $50\text{ }\mu\text{m}$ pitch. The size
117 of the active area is therefore $20.0\text{ cm} \times 16.8\text{ mm}$. This fine granularity allows for a high-precision
118 particle tracking. The chip operates at 40 MHz with a 25 ns acquisition window, which corresponds

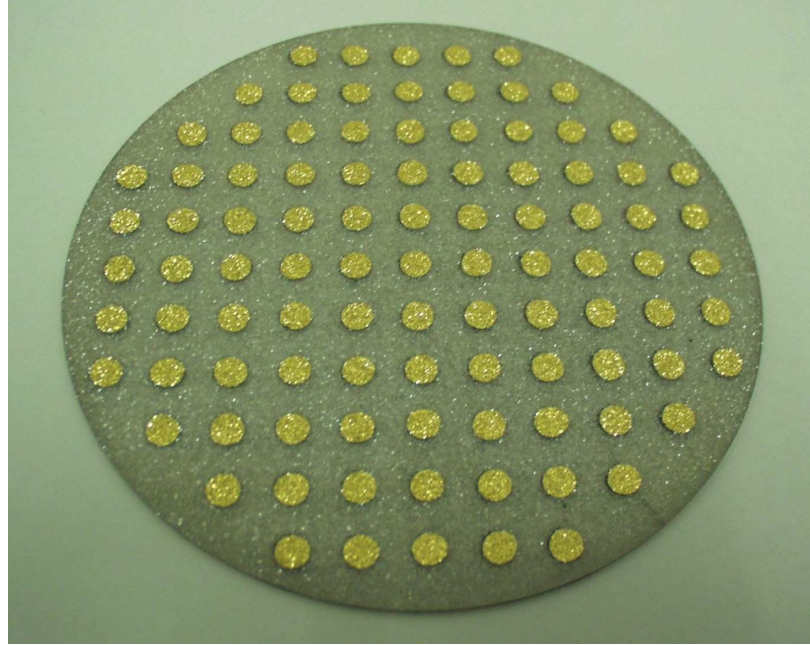


Figure 1.2: A pCVD wafer [?]. The golden dots on the surface are the electrodes that are applied during the qualification test. The wafer is measured across the surface to find the regions with the highest efficiency.

119 to the spacing of the particle bunches in the LHC. It is hence able to correlate hits/tracks to their
120 corresponding bunch. Furthermore, each pixel is capable of measuring the deposited charge of a
121 detected particle by using the Time-over-Threshold (ToT) method. Finally, the FEI4 has been
122 designed to withstand a radiation dose up to 300 MGy. This ensures a longterm stability in the
123 radiation hard forward region of the ATLAS experiment.

124 Each pixel is designed as a separate entity. Its electrical chain is shown in figure 1.4. The bump-
125 bond pad – the connection to the outside of the chip – is the input of the electrical chain, connected
126 to a free-running amplification stage with adjustable shaping using a 4-bit register at the feedback
127 branch. The analog amplifier is designed to collect negative charge, therefore electrons. The output
128 is routed through a discriminator with an adjustable threshold. This value in effect defines the level
129 at which the circuit detects a hit. In addition, there is a counter of the clock cycles (25 ns sampling)
130 during which the signal is above the discriminator threshold. The value of the counter is proportional
131 to the collected charge. The logic gates at the end of the chain are used to enable/disable the pixel
132 and to issue a so-called HitOr flag – this signal is set whenever at least one of the pixels was hit and
133 is used as a trigger for the readout. The output of the chain – HitOut – is routed into the logic of the
134 chip where it is buffered and sent out to the readout system. The module receives all its commands
135 from the system via a 40 MHz LVDS line. The commands are either settings for the pixel registers
136 or triggers that start the data readout. The data are sent via an LVDS line at up to 320 Mbit/s,
137 but by default at 160 Mbit/s, four times faster than the clock of the device. This allows the chip to
138 clear out its buffers before new data are recorded, thus avoiding dead time and data pile-up. The
139 FE-I4 has been successfully tested for trigger rates of up to 300 kHz, depending on the occupancy
140 per trigger.

141 The DBM uses pCVD diamond with $d_C = 500 \mu\text{m}$ thickness and silicon with $d_{Si} = 200 \mu\text{m}$
142 thickness as a sensor material. The resulting most probable value (MPV) of the deposited charge

1.3. DIAMOND PIXEL MODULE

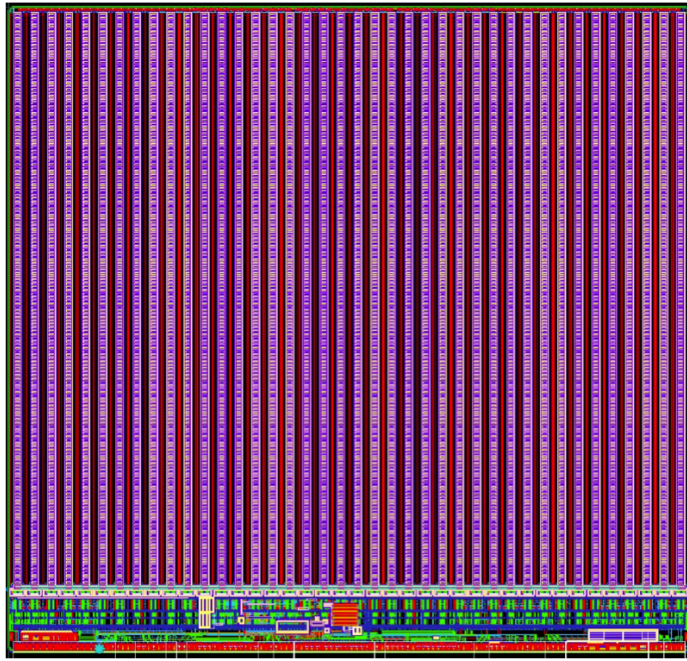


Figure 1.3: FE-I4 layout, top-down view. The pink area are pixels grouped into columns, the green area below is the common logic and the red strip at the bottom are the wire bond pads.

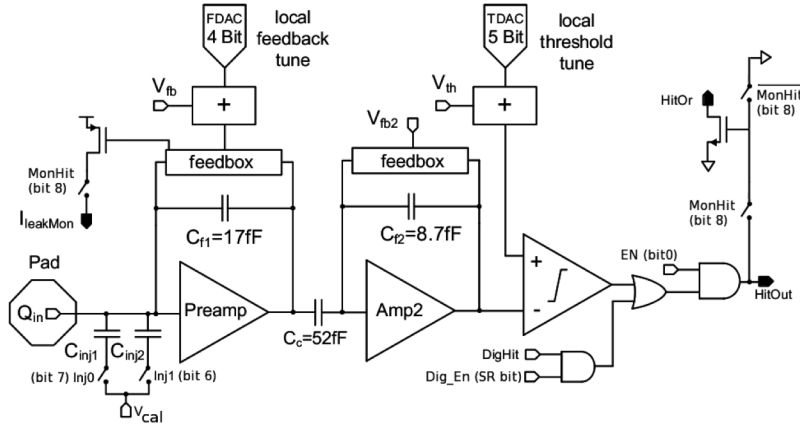


Figure 1.4: Schematic of an analog pixel. Courtesy of the FE-I4 collaboration.

for a minimum ionising particle (MIP) is calculated with the formula $Q_S = d \cdot E_{e-h}$ and equals 18'000 electrons and 17'800 electrons, respectively, at a full charge collection efficiency. This is not the case with the pCVD material, whereby the expected charge collection efficiency is of the order of 50 % – around 9'000 e. This value further decreases with received irradiation dose. Therefore in order to detect the particles depositing energy on the far left side of the Landau spectrum, the threshold has to be set to a significantly lower value. On the other hand, if the threshold is set too low, it also detects the electronic noise and generates false hits. Typical noise amplitudes are in the range of 120 e – 200 e. A safe threshold range is approximately five times above this value. The target for the DBM is to set the threshold to 800 e.

The analog amplifier is implemented in two stages to get a fast rise time at a low noise and a low

power consumption. The output signal of the analog amplifier has a triangular shape with a fast rise time and a long decay. The shape can be adjusted by tuning the amplifier feedback loop. Its length is proportional to the collected charge, but it needs to be calibrated first. This is done by means of two injection capacitors, $C_{\text{inj}1}$ and $C_{\text{inj}2}$, seen in figure 1.4 with well defined capacitances. First, the charge $Q_{\text{cal}} = V_{\text{cal}} \cdot (C_{\text{inj}1} + C_{\text{inj}2})$ is injected into the analog chain. Then the length of the output pulse is measured and finally the feedback value is changed to either lengthen or shorten the pulse in order to get to the required duration t_{cal} . The typical values are $Q_{\text{cal}} = 5'000 \text{ e} - 16'000 \text{ e}$ at the time $t_{\text{cal}} = 5 \text{ ToT} - 10 \text{ ToT}$. The target values depend on the sensor, the type of a radioactive source and the application. Therefore the initial threshold Th at 1 ToT and the calibrated value Q_{cal} at t_{cal} ToT give us a linear scale of collected charge with respect to time over threshold. However, in practice this relation is nonlinear for lower thresholds, but since the goal of the measurements is to track the particles rather than to measure their deposited energy precisely, this is sufficient.

1.4 Module assembly

Parts for the detector arrived separately and were assembled into modules at CERN’s DSF lab after being checked for production faults. The assembled modules underwent a series of quality control (QC) and burn-in tests to determine their quality, efficiency and long-term stability.

A DBM single-chip module consists of a hybrid pixel module, a flexible PCB and the supporting mechanics (a ceramic plate and an aluminium plate). The chip arrives already bump-bonded to the sensor, be it diamond or silicon. First it is glued to the ceramic plate on one side and to the PCB on the other using Araldite 2011 or Staystik 672/472. Staystik is re-workable and has a very high thermal conductivity. The latter is important because the FE-I4 chips tend to heat up significantly and need a good heat sink. The problem is that it has a curing temperature of 160/170 °C. This temperature may cause some unwanted stress build-up between the FE-I4 and the diamond sensor due to different coefficients of thermal expansion, pulling them apart. This would disconnect the pixels, yielding large regions of the module insensitive to radiation. Araldite 2011 on the other hand can be cured at lower temperatures – down to RT – but it has a lower heat conductivity. In the end Araldite is used as a safer option. However, due to the longer curing, the entire assembly process using Araldite is three times as long. After curing, the module is wire-bonded and attached to the aluminium plate using screws made up of a radiation-resistant PEEK polymer. They have to be tightened with a great care, because their screw head is only 0.2 mm – 0.6 mm away from the sensor edge – the sensor displacement tolerance during gluing is of the order of 0.5 mm. Finally, the module is put in an aluminium carrier which protects it from mechanical damage or electrostatic discharges. Figure 1.5 shows an assembled module.

1.5 Performance results

This section gives an overview of the performance results of the DBM modules achieved during the QC and the test beam campaign. The source tests were performed to check for disconnected regions in the sensors and to measure the diamond’s efficiency. Only the modules with minimal disconnected regions and maximum efficiency were chosen for installation.

1.5.1 Source test results

The modules are tested in the lab using an Reconfiguration Cluster Element readout system [6] and a moving stage with two degrees of freedom. They are placed onto the stage and connected to the

1.5. PERFORMANCE RESULTS

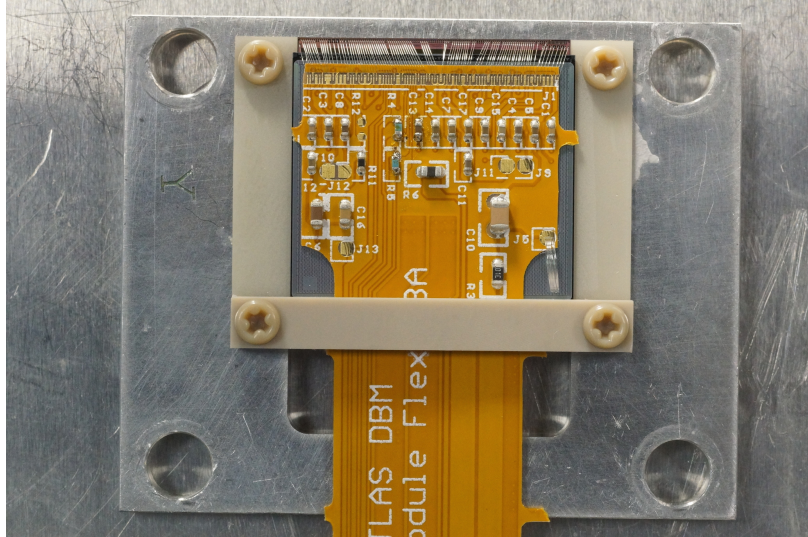


Figure 1.5: DBM module, top-down view. Visible is the flexible PCB with signal and power connections, the silicon sensor and a part of the FE-I4. Wire bonds from the PCB to the FE-I4 and to the sensor are also visible.

194 readout system and the power supplies. After ensuring the low- and high voltage connectivity they
195 are checked for the signal connectivity. If everything is operational, a series of automated tests is
196 run. Each of these tests calibrates a certain value within a pixel, whether it is the signal threshold
197 or the value for integrated charge. These are tuned in a way that the response to a predefined
198 calibration signal is uniform for all pixels across the sensor. This procedure is referred to as *tuning*.

199 When the modules are tuned, they are tested using a ^{90}Sr radioactive source. Two characteristics
200 of each module are checked: 1) operation of all pixels and 2) sensor efficiency.

201 Pixel connectivity

202 The first test is carried out to determine the number of disconnected pixels in the matrix. This
203 is an important step in the DBM QC procedure, because it turns out that a significant portion of
204 the flip-chipped diamond sensors exhibited very poor connectivity. The disconnected regions on the
205 faulty modules ranged anywhere from 0.1 % – 80 % of the overall active surface. In two cases the
206 sensor was even completely detached from the chip. Therefore the pixel connectivity turns out to
207 be the most important qualification factor in the QC procedure. However, the only way to check it
208 at the moment is to fully assemble a module and test it using a radioactive source. If the module
209 turns out to be of poor quality, it is disassembled and sent for rework. The turnover time of this
210 operation is of the order of one month, which affected the DBM installation schedule significantly.
211 In the end the modules with less than 3 % disconnected pixels have been accepted.

212 The test for disconnected regions is carried out by moving the module under the source in X
213 and Y direction so that the exposure over the entire plane is uniform. The resulting occupancy map
214 reveals pixels that are not electrically coupled to the sensor via bump bonds. The occupancy scans
215 are shown in figures 1.6a and 1.6b. The silicon module has a very uniform occupancy plot. So much
216 so that the features of the overlaying flexible PCB can be observed. The rectangular shadows are
217 the passive components whereas the lines are the traces in the PCB. Furthermore, a circular-shaped
218 edge of the PCB can be seen on the bottom right side of the plot. These darker areas are such
219 because fewer electrons can penetrate the material with a high density. In the case of the diamond,

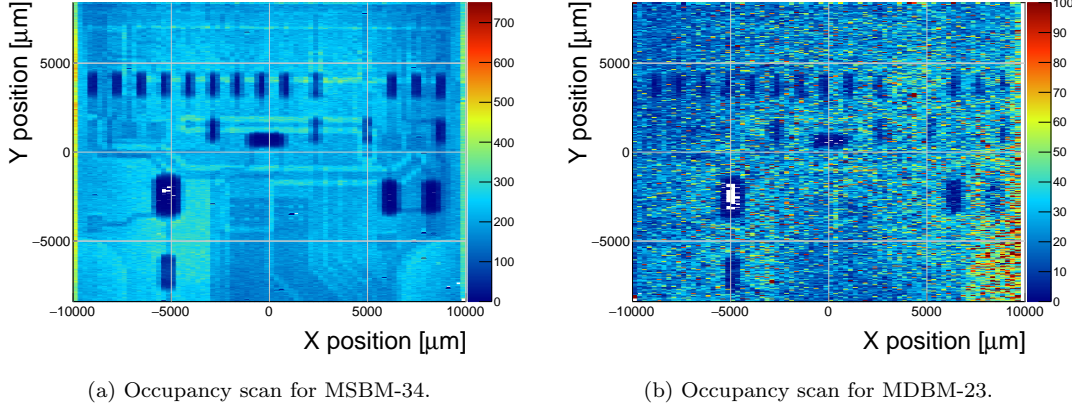


Figure 1.6: Occupancy scans for the silicon (left) and diamond sensor (right) to check for disconnected regions. Shadows of the electronic components are clearly visible because fewer electrons were able to traverse through such a higher amount of material.

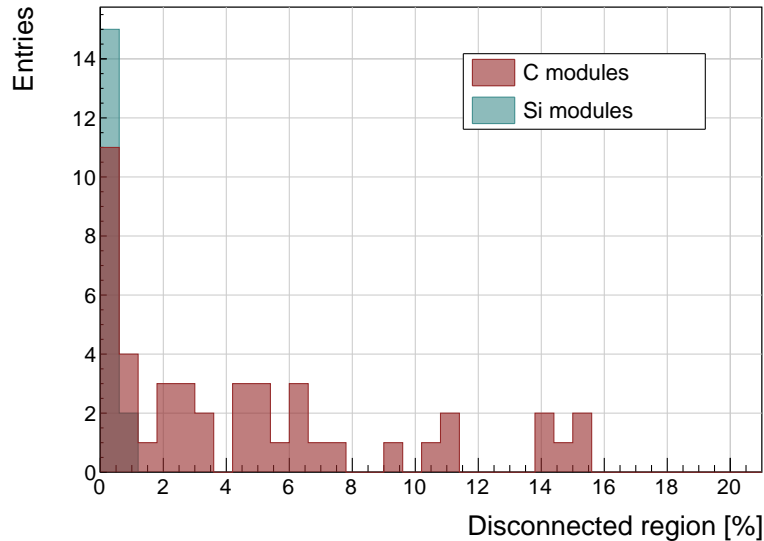


Figure 1.7: Disconnected regions for all modules derived from the occupancy scans.

the features of the PCB can be observed as well, but are much less distinguishable as the plot is much more granulated – less uniform. This high variance in the diamond’s detection ability is due to the grain boundaries in the pCVD material which trap the drifting charges, rendering some regions significantly less efficient.

Figure 1.7 shows the distribution of disconnected regions across all tested modules. Silicon modules were performing as expected, with a minimum number of disconnected pixels.

226 Pseudo-efficiency

Only the modules that passed the pixel connectivity test undergo the second test stage in which the sensor’s efficiency is estimated. A scintillator is placed underneath the module and is used as a trigger. A particle that crosses the DBM module and hits the scintillator, triggers the module

1.5. PERFORMANCE RESULTS

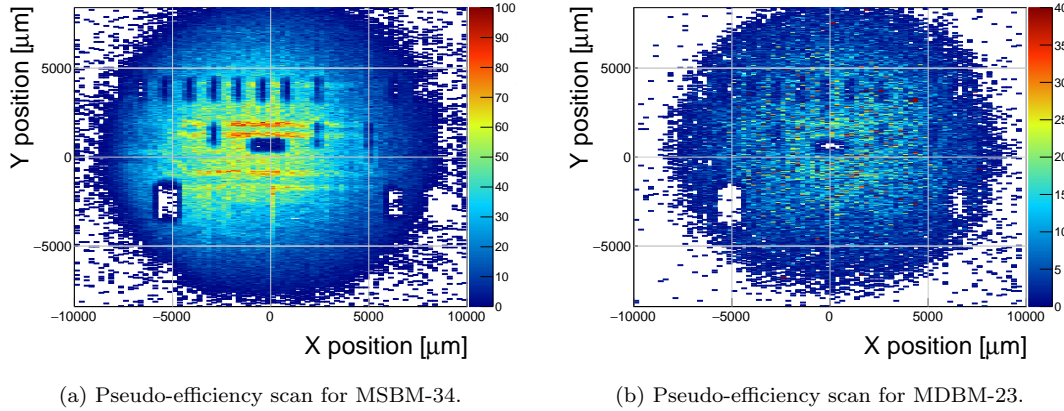


Figure 1.8: Pseudo-efficiency scans for the silicon (left) and diamond sensor (right) to estimate the efficiency of the sensors.

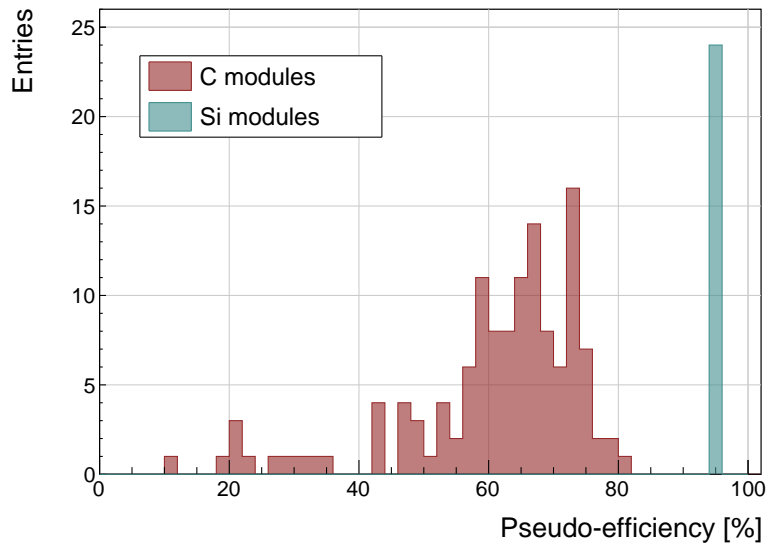


Figure 1.9: Pseudo-efficiencies for all modules at various threshold and voltage settings.

readout. In the end, the number of triggers is compared to the number of hits/clusters recorded by the module. These are shown in figures 1.8a and 1.8b.

However, the resulting ratio is only an estimate of the sensor's detection efficiency. This is because the β particles scatter around the setup and sometimes hit the scintillator from other directions without traversing the module, producing empty triggers. Therefore the real sensor efficiency can only be measured in a high energy particle beam and using a beam telescope as a reference detector to measure the particle trajectories. Nonetheless, this *pseudo-efficiency* gives a rough estimate of the sensor's quality.

Figure 1.9 shows the distribution of pseudo-efficiencies for all modules that went through the QC. The majority of the silicon modules yield the pseudo-efficiency of $(94.3 \pm 0.2)\%$. Silicon sensors being 99.99 % efficient, this value is underestimated by about 5 %. The measured pseudo-efficiency of the diamond modules is $(65 \pm 7)\%$, with outliers down to 10 %. The value depends on the diamond quality, the set threshold and the applied bias voltage. The latter two settings are varied

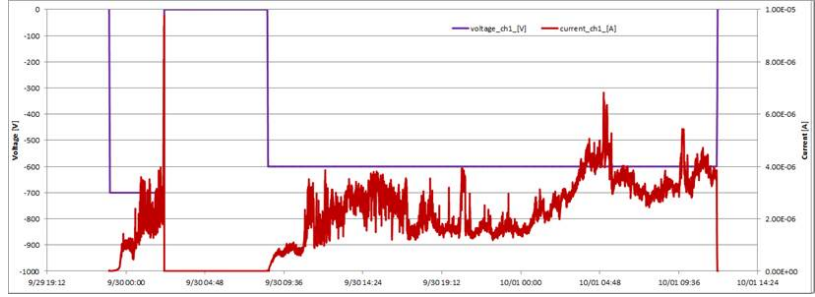


Figure 1.10: Erratic current in a DBM diamond module. The purple and the red signal line represent the applied bias voltage and the measured leakage current.

²⁴³ to check the behaviour of the modules under various conditions.

²⁴⁴ 1.5.2 Erratic current

²⁴⁵ A very important parameter for qualifying a module is the erratic current [12] in the sensor. This
²⁴⁶ term describes the leakage current in a pCVD diamond that becomes unstable. It can develop
²⁴⁷ gradually or can be triggered with a β source. Spikes appear in the otherwise stable leakage current.
²⁴⁸ They can be up to three orders of magnitude higher than the base current. Sometimes the current
²⁴⁹ also suddenly increases for a few orders of magnitude and stays at that level (e.g. from the initial
²⁵⁰ 1 nA to 3 μ A). An example of such behaviour is shown in figure 1.10.

²⁵¹ The amplitude differs in magnitude from sensor to sensor. This effect is still not fully explained,
²⁵² but the hypothesis is that the charges find a conductive channel along the grain boundaries, causing
²⁵³ discharges. These discharges are picked up by the pixel amplifiers in the FE-I4. A single discharge
²⁵⁴ can trigger a group of up to \sim 500 pixels, resulting in a *blob* on the detector occupancy map.
²⁵⁵ Sometimes the conductive channel stays in a conductive state, making one or more pixels always to
²⁵⁶ fire. These pixels saturate the bandwidth of the readout channel, so they have to be masked out
²⁵⁷ during measurements.

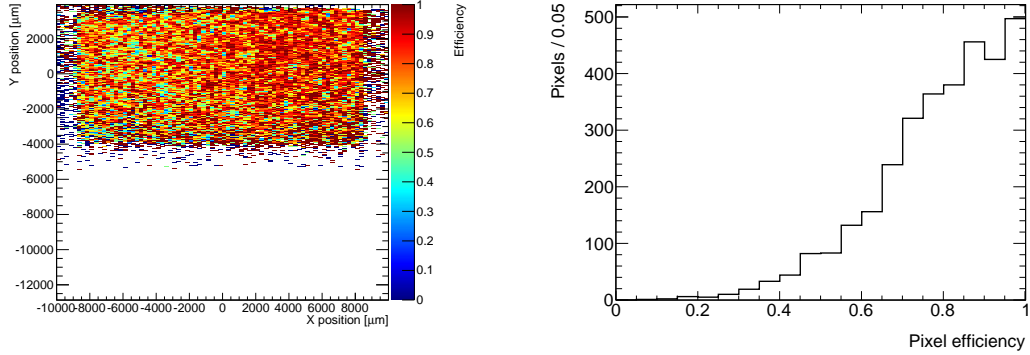
²⁵⁸ 1.5.3 Test beam results

²⁵⁹ The first two assembled prototype DBM modules, MDBM-01 and MDBM-03, were tested at DESY,
²⁶⁰ Hamburg, in a test beam facility. The aim of the measurements was to measure their efficiency, the
²⁶¹ spatial distribution of the efficiency and the effect of the beam on the disconnected regions. A silicon
²⁶² module MSBM-02 was measured to crosscheck the measurements. Since the silicon module is almost
²⁶³ 100 % efficient, it was used as an “anchor” – the efficiency of the diamond module was measured
²⁶⁴ relative to that of the silicon module. Two beam telescopes were used as reference systems: Kartel
²⁶⁵ telescope [11] built by JSI institute from Ljubljana, and EUDET Aconite [2]. Both are instrumented
²⁶⁶ with six Mimosa26 pixel planes and capable of tracking particles with a 2 μ m pointing resolution.

²⁶⁷ The test beam prototypes did not meet the acceptance criteria for production DBM modules in
²⁶⁸ the following areas: first, the stated CCDs were slightly below 200 μ m, which would be the DBM
²⁶⁹ minimum. Secondly, the applied bias voltages ranged from 1–2 V/ μ m. In addition, the threshold cut
²⁷⁰ could only be set to 1500 electrons, which is higher than the DBM minimum (1'000 e). Nonetheless,
²⁷¹ the resulting module efficiencies were still in the range between 70–85 %.

²⁷² To analyse the test beam data, Judith software framework [11] was used. Judith is capable
²⁷³ of synchronising data streams from several detector systems only connected via a trigger system,
²⁷⁴ reconstructing tracks and calculating efficiency for the DUTs. It was also used to reconstruct and

1.5. PERFORMANCE RESULTS



(a) This figure shows an efficiency map of ad DBM pVCD diamond module. Each bin corresponds to a single pixel. The triggering scintillator of the Kartel telescope is smaller than the DUT. Hence, the recorded hits can only be seen in the top half of the sensor.

(b) A pixel efficiency distribution from the run in figure (a).

Figure 1.11: An efficiency study of a prototype DBM diamond module in a test beam. The statistics are low (~ 10 hits/pixel) as the data were collected during a short run.

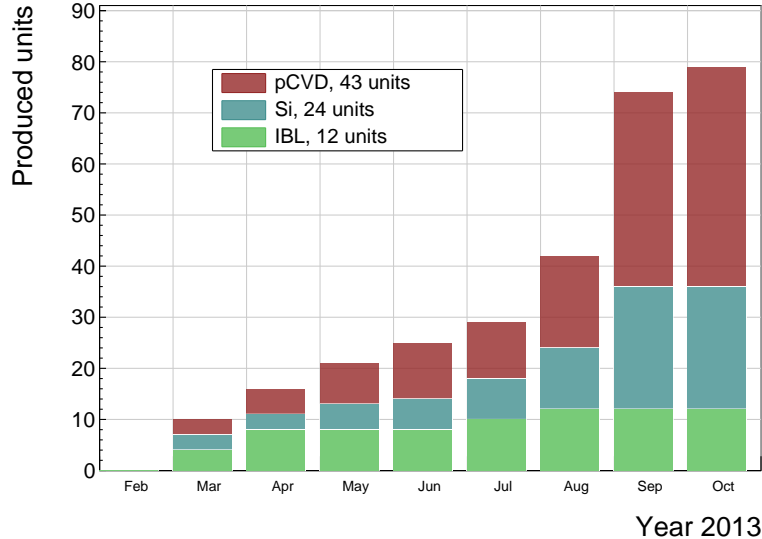


Figure 1.12: Module production with time.

275 analyse the acquired Kartel test beam data together with the silicon and diamond module as DUTs.
276 A sample of the analysed data is shown in figures 1.11a and 1.11b.

277 1.5.4 Summary of the QC

278 All in all, 79 modules went through the QC procedure – 43 diamond modules and 36 silicon modules,
279 12 of the latter only for testing purposes. Figure 1.12 shows their production with time. 18 diamond
280 modules and 6 silicon modules were in the end chosen to be integrated into DBM telescopes and
281 installed into ATLAS.



Figure 1.13: This photo highlights four telescopes installed onto the nSQPs and around the pipe.

282 1.6 Installation and commissioning

283 The DBM modules that passed the QC tests were assembled into telescopes – sets of three modules
284 one behind the other with a spacing of 50 mm. Of the 18 diamond and 6 silicon modules, 6
285 diamond and 2 silicon telescopes were built. A special care was taken when choosing the sets of
286 three diamonds. The modules with a similar pseudo-efficiency, leakage current, maximum stable high
287 voltage and shape of disconnected regions were grouped together. After assembly into telescopes, the
288 modules were tested for their connectivity. Then the high voltage was applied and the leakage current
289 was observed. This was an important point to check because all three modules shared the same high
290 voltage channel. Any instabilities on one of the modules would cause problems on the other two. This
291 would for instance happen if one of the modules had a much lower breakdown voltage. Due to time
292 constraints, the telescopes were not built at the same time but instead the production was pipelined.
293 As soon as two telescopes were ready, they were transported to Point 1 – the site where parts of
294 the ATLAS detector were being put together. There they were prepared for installation onto the
295 pixel detector structure that had been extracted from ATLAS due to pixel detector commissioning.
296 The commissioning was nearing completion, so the technicians were preparing the detector for re-
297 insertion. The cylindrical structure was being enclosed by four new service quarter-panels (nSQPs).
298 This meant that with every day the access to the place of installation of the DBM was more
299 difficult. The first two telescopes were still put into place when only one nSQP was in place. This
300 allowed the installation process to be carried out from both sides. This proved to be helpful, because
301 the process was lengthy and had to be done with great precision. It involved tightening several
302 screws on both sides of the telescopes, adding thermal paste on the aluminium joints and removing
303 the protective covers, revealing the fragile wire bonds. At the same time the surrounding electronics
304 and cables had to be left untouched. The lessons learnt with the first part of the installation were
305 helpful when installing the other telescopes. The last two were fitted onto the structure when three
306 nSQPs were already in place, leaving only a narrow opening for access. The entire procedure was
307 carried out blind. After every installation, the telescopes were tested again. First, the low voltage

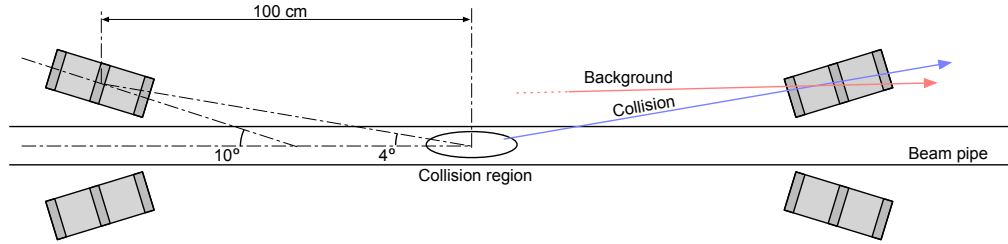


Figure 1.14: Position of the DBM in the ATLAS experiment.

308 connectivity was checked and a set of tests was run on the FE-I4 front-end chips. An eye diagram
 309 was made to estimate the quality of the signal transmission. Then a ^{90}Sr source was used to perform
 310 a source test on three modules at the same time. Leakage current was observed during the source
 311 test. The final test included running four telescopes (all on one side) at a time. All the tests were
 312 successful and the DBM was signed off.

313 1.6.1 Positioning in ATLAS

314 The DBM is placed in the forward region of the ATLAS detector very close to the beam pipe,
 315 as shown in figure 1.14. Eight DBM telescopes reside approximately 1 m away from the collision
 316 region, four on each side. They are tilted with respect to the beam pipe for 10°. This is due to
 317 a specific phenomenon connected to erratic (dark) currents in diamond. Studies have shown [12]
 318 that the erratic leakage currents that gradually develop in diamond can be suppressed under certain
 319 conditions.

320 For instance, if a strong magnetic field is applied perpendicular to the electric field lines in the
 321 diamond bulk, the leakage current stabilises. The DBM was designed to exploit this phenomenon.
 322 The magnetic field lines in the ATLAS experiment are parallel to the beam. Hence, an angular
 323 displacement of the sensor with respect to the beam allows for the leakage current suppression.
 324 However, the DBM telescopes still need to be directed towards the interaction region. Taking these
 325 considerations into account, a 10° angle with respect to the beam pipe was chosen. The influence of
 326 the magnetic field on the particle tracks at this angle is very low as the field lines are almost parallel
 327 to the tracks. The tracks are therefore straight, which reduces the track reconstruction complexity.

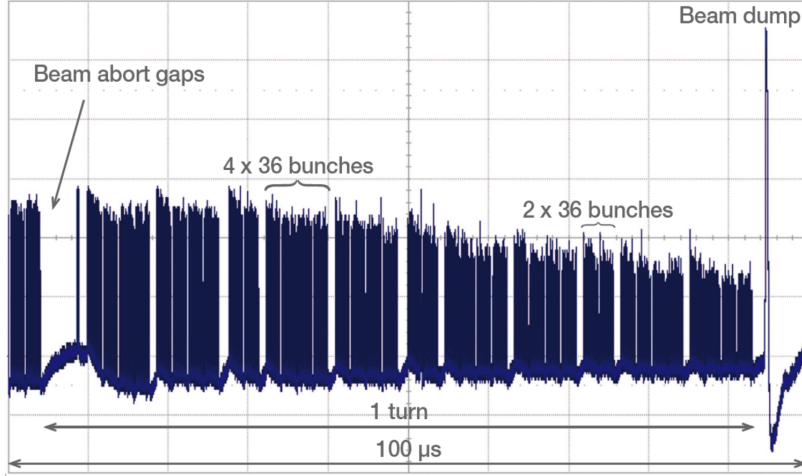


Figure 1.15: Time-resolved bunch structure at the LHC measured by diamond detectors [8]. The beam abort gap is clearly visible.

³²⁸ 1.7 First data taking during collisions

³²⁹ The detector's capability of particle tracking has been tested during collisions. Only one telescope
³³⁰ was used to take data.

³³¹ 1.7.1 LHC beam bunch structure

³³² As described in chapter ??, the LHC accelerates two beams of protons in opposite directions, in-
³³³ tersecting at four collision points. Collisions take place in a collision region around the nominal
³³⁴ collision point, with a gaussian spread. The particles in the beam are grouped in bunches. Not all
³³⁵ bunch buckets are filled, as shown in a time-resolved plot in figure 1.15. Therefore some bunches
³³⁶ arriving at the collision point do not have their corresponding bunches traveling in the opposite di-
³³⁷ rection. These are referred to as non-colliding or *unpaired bunches* while those with their respective
³³⁸ bunches in the opposite direction are *paired*. The unpaired bunches should not create any collisions.
³³⁹ Nevertheless, some collisions might still be detected, whether as a result of stray particles hitting
³⁴⁰ the beam pipe or the surrounding detectors or if the purportedly empty buckets still contain a small
³⁴¹ number of particles.

³⁴² 1.7.2 Collision point reference system

³⁴³ If all three planes of the telescope are hit during a bunch crossing, a linear line is fitted to these hits
³⁴⁴ and extrapolated towards the interaction region. This line represents the particle's trajectory. Two
³⁴⁵ parameters are calculated: the radial distance R_0 and the longitudinal distance Z_0 between the line
³⁴⁶ and the interaction point, as shown in figure 1.16. R_0 and Z_0 values at minimal d_0 are therefore the
³⁴⁷ cylindrical coordinates of the minimal distance between the particle's trajectory and the nominal
³⁴⁸ interaction point. Figure 1.17 shows the theoretical gaussian distribution of R_0 and Z_0 (black) as
³⁴⁹ well as the expected distribution as measured by one DBM telescope (blue). The latter is biased due
³⁵⁰ to the positioning and the aperture of the telescope. The red distribution shows the contribution of
³⁵¹ the particles colliding with the beam pipe and the surrounding electronics, such as the IBL [5].

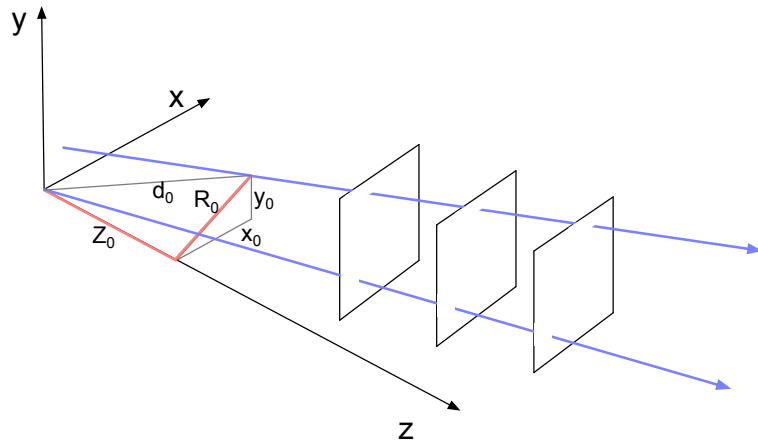


Figure 1.16: Two particle tracks. One originates in the centre of the collision region. The vertex of the other is at the radial distance R_0 and longitudinal distance Z_0 from the interaction point. Axis z is the beam direction. Three module planes intercept the particles and reconstruct their trajectory. The arrow on the top right shows the telescope used for data acquisition.

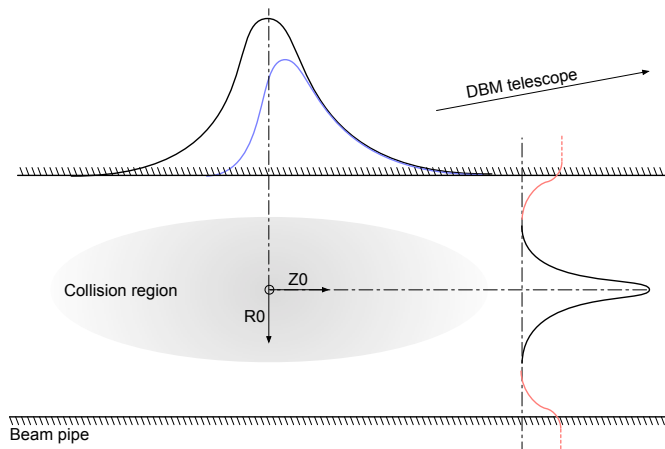


Figure 1.17: Distribution of collisions in the collision region. A single DBM telescope taking data records the collisions with a biased distribution marked blue. The red distributions stem from collisions of particles with the beam pipe or surrounding material.

1.7.3 Discussion

The data acquired with a single DBM telescope are shown in figures 1.18a and 1.18b. Histograms for collisions of paired and of unpaired bunches are plotted separately for each of the two cylindrical coordinates. For the colliding bunches, the majority of the reconstructed tracks has the origin close to the nominal interaction point, with a narrow spread in Z and R . A slight negative displacement in R_0 and a positive displacement in Z_0 are expected due to the positioning of the telescope.

For non-colliding bunches, the spread is wider. The R_0 distribution has one peak in the middle, which means that the empty buckets still hold some particles which collide. The two peaks on the sides, however, show that a significant number of tracks has their origin at the radius of the beam pipe. Therefore these tracks are made by stray protons colliding with the beam pipe and the

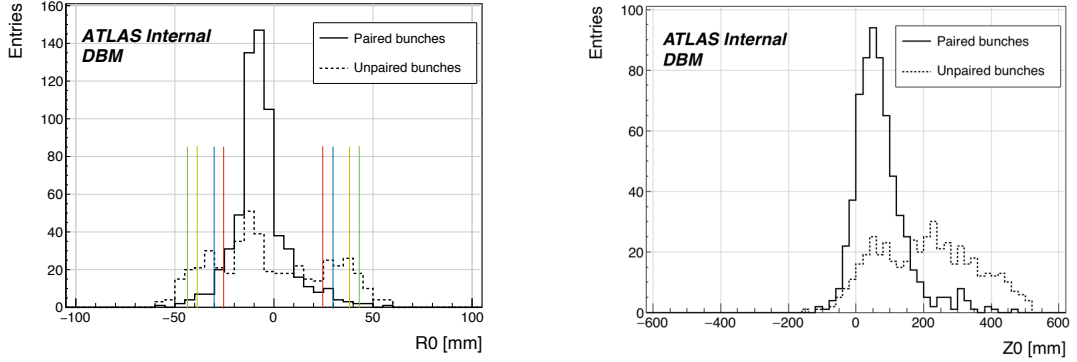


Figure 1.18: These two plots show two parameters of particle tracks recorded by one of the DBM telescopes: radial (left) and longitudinal (right) distance of the projected tracks from the interaction point. Note the different scale on the x axis. The red, blue, yellow and green lines mark the inner and outer radius of the beam pipe, the outer radius of the IBL and the outer radius of the IBL insertion tube [7, 5].

³⁶² surrounding material. These collisions are unwanted as they do not produce any meaningful physics
³⁶³ while still damaging the ATLAS detector by means of the scattered radiation. The Z_0 distribution
³⁶⁴ has a high spread in the positive direction. This bias is due to the positioning of the telescope. The
³⁶⁵ peak that coincides with that of the paired bunches stems from collisions of stray particles. The
³⁶⁶ second peak with a wide spread is due to collisions with the surrounding material.

³⁶⁷ 1.8 Conclusion

³⁶⁸ The Diamond Beam Monitor has been designed as an upgrade to the existing luminosity detectors
³⁶⁹ in the ATLAS experiment. It is the first diamond pixel tracking detector installed in a high-energy
³⁷⁰ physics experiment. The pixelated front-end electronic chips ensure precise spatial detection of the
³⁷¹ charged high-energy particles. The projective geometry allows for particle tracking and background
³⁷² rejection. The detector is placed in a high-radiation forward region of the experiment. Therefore,
³⁷³ radiation hardness of the chosen pCVD diamond sensors is an important requirement. The tests
³⁷⁴ carried out in the test beam and in the laboratory confirmed that enough detector-grade DBM
³⁷⁵ modules have been built to be installed in the experiment. The DBM is has been running in ATLAS
³⁷⁶ since October 2013.

377

Bibliography

- 378 [1] *CiS Forschungsinstitut fuer Mikrosensorik GmbH.* <http://www.cismst.org/>.
- 379 [2] *EUDET ACONITE telescope.* <https://telescopes.desy.de>.
- 380 [3] *Measurement of the Rate of Collisions from Satellite Bunches for the April-May 2010 LHC*
381 *Luminosity Calibration.* Technical Report ATLAS-CONF-2010-102, CERN, Geneva, Dec 2010.
- 382 [4] J et al. Albert. *Prototype ATLAS IBL Modules using the FE-I4A Front-End Readout Chip.*
383 *J. Instrum.*, 7(arXiv:1209.1906):P11010. 45 p, Sep 2012. Comments: 45 pages, 30 figures,
384 submitted to JINST.
- 385 [5] M Capeans, G Darbo, K Einsweiller, M Elsing, T Flick, M Garcia-Sciveres, C Gemme, H Pernegger,
386 O Rohne, and R Vuillermet. ATLAS Insertable B-Layer Technical Design Report. Technical
387 Report CERN-LHCC-2010-013. ATLAS-TDR-19, CERN, Geneva, Sep 2010.
- 388 [6] Richard Claus. *A New ATLAS Muon CSC Readout System with System on Chip Technology*
389 *on ATCA Platform.* Jun 2015.
- 390 [7] J Dopke. Overview of the ATLAS Insertable B-Layer (IBL) Project. Jul 2013.
- 391 [8] E. Griesmayer et al. *Diamond detectors for LHC. Proceedings for IBIC2012. Tsukuba, Japan,*
392 2012.
- 393 [9] A Gorišek, V Cindro, I Dolenc, H Frais-Klbl, E Griesmayer, H Kagan, S Korpar, G Kram-
394 berger, I Mandic, M Meyer, M Mikuz, H Pernegger, S Smith, W Trischuk, P Weilhammer, and
395 M Zavrtanik. *ATLAS diamond Beam Condition Monitor.* *Nucl. Instrum. Methods Phys. Res.,*
396 *A*, 572(1):67–69, 2007.
- 397 [10] Fabian Huegging. *The ATLAS Pixel Insertable B-Layer (IBL).* *Nucl. Instrum. Methods Phys.*
398 *Res., A*, 650(arXiv:1012.2742):45–49. 7 p, Dec 2010. Comments: 7 pages, 5 figures, 4 tables,
399 accepted by Nuclear Instruments and Methods A for publication.
- 400 [11] Garrin McGoldrick, Matevž Červ, and Andrej Gorišek. *Synchronized analysis of testbeam data*
401 *with the Judith software.* *Nucl. Instrum. Methods Phys. Res., A*, 765:140–145, 2014.
- 402 [12] S Mueller, W deBoer, M Schneider, A Sabellek, M Schmanau, C Ruehle, T Schneider, and
403 R Hall-Wilton. *Study of leakage currents in pCVD diamonds as function of the magnetic field.*
404 *Phys. Status Solidi, A*, 206(arXiv:0905.0403):2091–2097. 6 p, May 2009. Comments: 6 pages,
405 16 figures, poster at Hasselt Diamond Workshop, Mar 2009.
- 406 [13] Matevž Červ. *The ATLAS Diamond Beam Monitor.* Technical Report ATL-INDET-PROC-
407 2013-021, CERN, Geneva, Nov 2013.